Rocking curve imaging of high quality sapphire crystals in backscattering geometry

A. Jafari, I. Sergueev, D. Bessas, B. Klobes, B. S. Roschin, V. E. Asadchikov, P. Alexeev, J. Härtwig, A. I. Chumakov, H.-C. Wille, and R. P. Hermann

Citation: Journal of Applied Physics **121**, 044901 (2017); doi: 10.1063/1.4974106
View online: http://dx.doi.org/10.1063/1.4974106
View Table of Contents: http://aip.scitation.org/toc/jap/121/4
Published by the American Institute of Physics

Articles you may be interested in

Economies of scale: The physics basis
Journal of Applied Physics **121**, 044907 (2017); 10.1063/1.4974962

Dynamic fragmentation of Al-W granular rings with different mesostructures
Journal of Applied Physics **121**, 045901 (2017); 10.1063/1.4973730

Structural and magnetic properties of ultra-thin Fe films on metal-organic chemical vapour deposited GaN(0001)
Journal of Applied Physics **121**, 043904 (2017); 10.1063/1.4973956

Investigation of gate leakage current mechanism in AlGaN/GaN high-electron-mobility transistors with sputtered TiN
Journal of Applied Physics **121**, 044504 (2017); 10.1063/1.4974959

Universal field dependence of conventional and inverse magnetocaloric effects in $DyCo_2Si_2$
Journal of Applied Physics **121**, 043901 (2017); 10.1063/1.4974302

Theoretical simulation of negative differential transconductance in lateral quantum well nMOS devices
Journal of Applied Physics **121**, 044501 (2017); 10.1063/1.4974469


AIP | Journal of Applied Physics

Save your money for your research.
It's now FREE to publish with us -
no page, color or publication charges apply.

Publish your research in the
Journal of Applied Physics
to claim your place in applied
physics history.

JOURNAL OF APPLIED PHYSICS **121**, 044901 (2017)

Rocking curve imaging of high quality sapphire crystals in backscattering geometry

A. Jafari,[1,2,3] I. Sergueev,[4] D. Bessas,[2,a)] B. Klobes,[1] B. S. Roschin,[5] V. E. Asadchikov,[5,6] P. Alexeev,[1,4] J. Härtwig,[2,7] A. I. Chumakov,[2] H.-C. Wille,[4] and R. P. Hermann[1,3,8,b)]
[1]*Jülich Centre for Neutron Science JCNS and Peter Grünberg Institute PGI, JARA-FIT, Forschungszentrum Jülich GmbH, D-52425 Jülich, Germany*
[2]*ESRF- The European Synchrotron, CS40220, F-38043 Grenoble Cedex 9, France*
[3]*Faculté des Sciences, Université de Liège, B-4000 Liège, Belgium*
[4]*Deutsches Elektronen-Synchrotron, D-22607 Hamburg, Germany*
[5]*Shubnikov Institute of Crystallography RAS, Leninskii pr-t 59, Moscow 119333, Russia*
[6]*Lomonosov Moscow State University, Faculty of Physics, GSP-1, 1-2 Leninskiye Gory, Moscow 119991, Russia*
[7]*Department of Physics, Faculty of Science, University of Johannesburg, Johannesburg, South Africa*
[8]*Materials Science and Technology Division, Oak Ridge National Laboratory, Oak Ridge, Tennessee 37831, USA*

(Received 5 November 2016; accepted 2 January 2017; published online 23 January 2017)

We report on the characterization of high quality sapphire single crystals suitable for high-resolution X-ray optics at high energy. Investigations using rocking curve imaging reveal the crystals to be of uniformly good quality at the level of $\sim 10^{-4}$ in lattice parameter variations, $\delta d/d$. However, investigations using backscattering rocking curve imaging with a lattice spacing resolution of $\delta d/d \sim 5 \times 10^{-8}$ show very diverse quality maps for all crystals. Our results highlight nearly ideal areas with an edge length of 0.2–0.5 mm in most crystals, but a comparison of the back reflection peak positions shows that even neighboring ideal areas exhibit a relative difference in the lattice parameters on the order of $\delta d/d = 10\text{–}20 \times 10^{-8}$; this is several times larger than the rocking curve width. Stress-strain analysis suggests that an extremely stringent limit on the strain at a level of $\sim$100 kPa in the growth process is required in order to produce crystals with large areas of the quality required for X-ray optics at high energy. *Published by AIP Publishing.*
[http://dx.doi.org/10.1063/1.4974106]

I. INTRODUCTION

White sapphire, i.e., α–Al_2O_3 corundum, single crystals have excellent pressure and temperature stability, extreme hardness, high transparency, and high dielectric constant. As such they are suitable for many advanced optical applications such as medical lenses,[1] light-emitting diodes,[2] electronic substrates,[3,4] and focusing devices.[5,6] Sapphire is a promising candidate for hard X-ray optical applications,[7] high pressure cells for neutron scattering experiments,[8,9] and optical windows in corrosive atmospheres.[10,11] Sapphire single crystals with low- to medium- optical quality can satisfy many demands whereas routine production in the highest quality is still an unreached milestone. An emerging application of sapphire is relevant to X-ray monochromatization. Currently, common X-ray monochromators based on silicon and germanium have significant limitations for application in X-ray inelastic scattering due to their high crystal symmetry. For Resonant Inelastic X-ray Scattering (RIXS) and Nuclear Resonant Scattering (NRS), the relevant probe beam energies are defined by the elemental absorption edge and by specific nuclear resonance energies, respectively. Unfortunately in most cases, the probe beam energy cannot be chosen to match energies favorable for Si-based optics. Both the RIXS and Nuclear Inelastic Scattering (NIS) (sometimes referred to as nuclear resonant inelastic x-ray scattering (NRIXS)) methods require X-ray optics as analyzers[12] or monochromators[13] based on low symmetry crystals such as α-quartz or sapphire, crystals which enable a quasi-continuous choice of high resolution X-ray beams. For NIS, sapphire is currently the only high-efficiency choice being explored for energies above 30 keV because of the high Debye-Waller factor that ensures high reflectivity. Note that multiple-crystal Si monochromators often used at 10–25 keV are possible for a few particular energies above 30 keV,[14] however, with comparatively very limited spectral reflectivity.

Several nuclear transitions with energies above 30 keV can be investigated by NIS, in particular, the transitions of ^{125}Te at an energy of 35.49 keV,[15,16] of ^{121}Sb at 37.13 keV,[16,17] and of ^{129}Xe[18] at 39.6 keV. Theoretical calculations[13] predict for the sapphire backscattering monochromator an energy bandwidth of 0.3–0.7 meV, i.e., $\delta E/E = 1\text{–}2 \times 10^{-8}$ for these energies. In 2005, the first Nuclear Forward Scattering (NFS) signal at 37.13 keV (^{121}Sb nuclear transition) using a sapphire backscattering monochromator was recorded at the nuclear resonance scattering beamline, ID18 at the ESRF,[19] with a 7 meV bandwidth.[20] In 2007, NIS at the same energy with an improved resolution of 4.5 meV was reported.[17] NIS experiments at 35.49 keV

[a)] Present address: Fundamental Aspects of Materials and Energy, Department of Radiation Science and Technology, Delft University of Technology, Mekelweg 15, 2629 JB Delft, The Netherlands

[b)] Author to whom correspondence should be addressed. Electronic mail: hermannrp@ornl.gov

(^{125}Te nuclear transition) have been carried out with 7.5 and 6.6 meV energy resolution at BL09XU at SPring-8[21] and at the nuclear resonance scattering station ID22N, ESRF,[15] respectively. Thus, attempts to use sapphire as a high resolution monochromator for NIS show that the main limiting factor is the quality of available crystals, which is ten times worse than the theoretical expectation. It was shown that it is possible to achieve $\delta E/E \sim 2 \times 10^{-8}$ using particularly small volumes in the best crystal,[16] at the cost of additional focusing optics. Energy bandwidths of 1.2, 1.1, and 0.95 meV were obtained at 37.13,[16] 35.49,[16] and 39.6 keV (Ref. 18) (^{121}Sb, ^{125}Te, and ^{129}Xe nuclear transitions), respectively. However, the possibility to reproduce the same resolution with other sapphire crystals and achieving the theoretical energy resolution, which is factor 2 better than in the previous studies, is questionable.

The difficulty in growing sapphire crystals can be related to a binary composition requiring two elements, Al and O, as compared to the crystals like silicon requiring only one element. Also, molten sapphire has a high viscosity,[22] $\eta = 1.8 \times 10^{-5}$ m^2 s^{-1}, that may allow lattice defects to form more easily than the low viscosity of, e.g., silicon[23] with $\eta = 3 \times 10^{-7}$ m^2 s^{-1}. Furthermore, the relatively high melting temperature of 2030 K certainly makes the control of thermal gradients more challenging. The quality of the sapphire crystals clearly depends on the production method. A wide range of growth techniques have been refined, such as Czochralski, Kyropoulos, and heat exchanger methods, in order to overcome the crystal quality problems related to growth issues.[2,24,25] The crucible and insulation material, the purity of the raw material, the growth rate and temperature gradient control are the main parameters for the growth of high-quality crystals. Several numerical analysis studies of the Kyropoulos technique estimating the temperature gradient, the temperature of the reactor,[24] and the thermal stress distribution[26] have aimed at defining how to produce improved sapphire crystals. These studies reveal high thermal stresses at the interface between the seed and crystal as well as at the shoulder and at the bottom part of the boule. Limited improvements have been achieved and extensive reviews on sapphire growth and applications are documented.[27,28]

Quantifying and understanding imperfections in single crystals calls for advanced characterization methods. Their non-destructive nature makes several X-ray based techniques well suited. X-ray diffraction topography using either a polychromatic (white radiation) or a monochromatic beam is an imaging technique based on Bragg diffraction.

The rocking curve evaluation with a monochromatic beam is one of the most commonly used techniques for quantitative measurement of crystalline perfection, with one of the first studies of rocking curves being a measurement of a ruby crystal (Al_2O_3) documented in 1965.[29] Adams *et al.* reported the effects of dislocations, residual grinding, polishing, mosaic structure, and twinning on the crystal quality.[30] Quality assessment of several sapphire substrates revealed a full width at half maximum (FWHM) of the rocking curves in the range of a few tens of arc-sec to arc-min.[30] In the following, all angular and energy widths will be quoted as FWHM. A combination of X-ray diffraction rocking curves and atomic force microscopy (AFM) showed that sapphire wafers treated with chemo-mechanical polishing with subsequent chemical etching have better surface smoothness compared to those treated only by mechanical polishing or by chemo-mechanical polishing.[31] Nowadays, a large number of topographs can be recorded by a CCD camera in a Rocking Curve Imaging (RCI) setup at synchrotron radiation facilities.[32] These topographs can be analyzed with software that enables automatic high-speed treatment of large data volumes to reveal a wealth of spatially resolved information.

Sapphire single crystals suitable as high resolution monochromators require quantitative RCI with a resolution of $\delta d/d \sim 10^{-7}$–10^{-8}, which corresponds to the theoretically expected $\delta E/E$. Such high sensitivity requires Bragg reflections with a small width of 0.02–0.2 arcsec (Ref. 33) if the Bragg angle is not within a few tenths of a degree of 90°. These measurements are challenging even with synchrotron radiation sources. One way to achieve the required sensitivity is to use backscattering RCI, where the investigated crystal is installed in backscattering diffraction geometry and the rocking curve measurements are performed by variation of the incoming X-ray energy using multiple-crystal Si high-resolution monochromators (HRM) with $\delta E/E \sim 3$–6×10^{-8}. In backscattering geometry, reflections with the Bragg angle very close to 90° are used. The advantage of backscattering RCI is that due to the large angular acceptance of the back reflections, the reflectivity becomes insensitive to the lattice inclination and depends only on the lattice variation $\delta d/d$.

By taking advantage of the features of the RCI and the backscattering geometry, the intrinsic energy widths of the reflectivity curves have been evaluated with a resolution of $\delta E/E \sim 10^{-7}$–10^{-8} in quartz,[34] diamond,[35] and sapphire.[16] The last study has evaluated imperfections in *C*-plane sapphire crystals, i.e., with [0 0 0 1] direction as surface normal, (*hkil*) indices are given for the sapphire reflections, where $i = -(h+k)$, with a small beam of 0.1×0.2 mm^2 and a spatial resolution of 0.4 mm using slits after a high resolution monochromator operating at 23.9 keV.[16] The sapphire crystal studied in Ref. 16 has a few high quality regions that make it suitable as a backscattering monochromator at beamline ID18, ESRF.

In this study, we report on the quality assessment of sapphire crystals with the purpose of monochromatization of a synchrotron X-ray beam at high energies. We show a quantitative analysis of the crystalline quality using different topography techniques and in particular, demonstrate the use of high-throughput backscattering RCI over large areas with a spatial resolution of 55 μm. We found small areas with almost perfect crystallites in several crystals. A relative stress in the order of 40(5) kPa is determined, stress which causes displacements in *d*-spacing even in these nearly ideal crystallites.

II. EXPERIMENTAL

We investigated the quality of five sapphire single crystals grown by the Kyropoulos and Bridgman techniques, see crystal details in Table I. These crystals were grown in the Shubnikov Institute of Crystallography in Moscow and

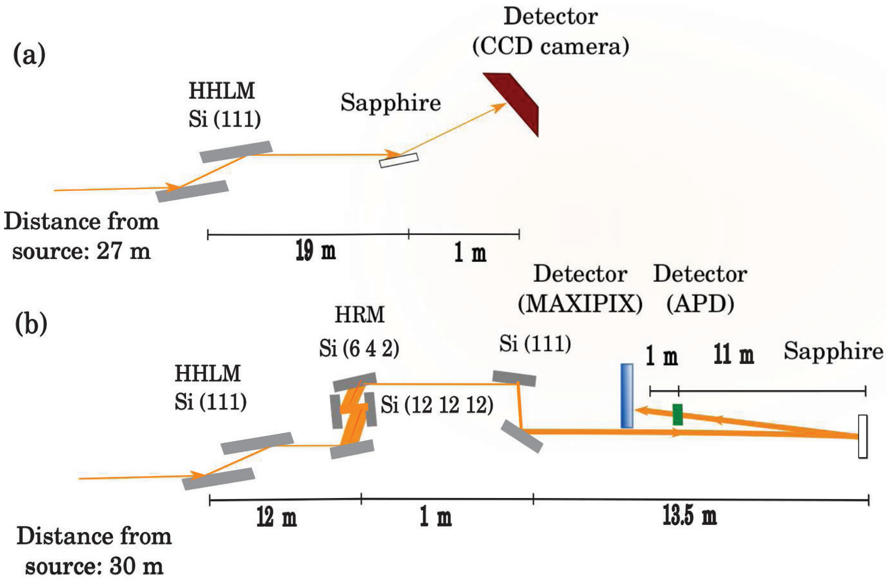

FIG. 1. (a) A schematic representation of the setup of the rocking curve imaging at BM05, ESRF. A silicon high heat load monochromator (HHLM) of two Si(111) reflections was used to adjust the synchrotron radiation to an energy of 20 keV. The sapphire was located close to the CCD detector. (b) Schematic view of the backscattering RCI experimental setup at ID18, ESRF. Starting left and following the beam (yellow): high heat load monochromator, high-resolution monochromator (HRM), asymmetrically cut Si(111) crystals with $b_{\mathrm{total}} = 10$, the sapphire crystal under study, avalanche photo-diode (APD) detector, and MaxiPix detector. The diffracted intensity from back reflections of sapphire has been recorded by the MaxiPix detector after moving the APD detector out of the beam.

selected from a batch studied by white beam topography (WBT), reported in Ref. 36.

First, crystal #1 was characterized by RCI at beamline BM05, ESRF. The schematic setup for this experiment is shown in Fig. 1(a). In the RCI setup, the 20 keV beam coming from the silicon high heat load monochromator (HHLM) with chosen Si(1 1 1) reflections is diffracted by the sapphire when it fulfills the Bragg condition of the reflection (0 0 0 6) with Bragg angle 8.2°. The intrinsic angular width of this reflection is about 0.3 arcsec. However, due to the mismatched Bragg angles of Si(111) and sapphire (0 0 0 6), the energy bandwidth of the upstream monochromator and incoming beam divergence affect the rocking curve width. The numerical calculations provide the rocking curve width for the ideal sapphire crystal to be 4 arcsec taking into account an energy bandwidth of 2.8 eV and a beam divergence up to 15 μrad. At the same time, the bandwidth of the monochromator varies with the heat load and static curvature of the monochromator crystals and could be smaller than expected. Thus, 4 arcsec can be considered as an estimated value for the expected rocking curve width, which gives a characteristic sensitivity of the method to the lattice spacing[33] as $\delta d/d = \Gamma/\tan\theta_B \sim 10^{-4}$, where Γ is the experimentally measured rocking curve width measured in the experiment. Whereas the expected width of the rocking curve depends on the monochromator properties, the relative changes of the rocking curve widths, measured under the same experimental conditions, reveal relative changes in the crystal quality.

The pre-characterization with a standard setup at BM05, ESRF, enabled us to obtain a general overview of the crystalline quality of the selected crystal and enabled both comparison with earlier studies and correlation with the other methods. As expected, the sensitivity of this set-up is sufficient for applications requiring medium quality sapphires but insufficient for high-resolution applications.

An image is recorded in the CCD detector for each angular step of ~0.9 arcsec. By rocking the sapphire crystal, sequences of topographs were recorded and then assembled to yield a topograph of the entire crystal. We used the Visrock program for numerical analysis of sequences of digital X-ray images.[37]

The same crystal was studied using white beam topography in transmission geometry using a large beam size in order to assess the overall quality across the crystals and to visualise possible macroscopic defects such as dislocations or inclusions. This study was performed at BM05, ESRF.

The schematic backscattering RCI setup designed at the beamline ID18, ESRF, is depicted in Fig. 1(b). The beam after the HHLM was further monochromatized by a multiple-crystal channel-cut Si HRM[38] consisting of two

TABLE I. Characteristics of the investigated sapphire crystals, the Bragg reflection, and the incident photon energy used to measure each crystal in backscattering RCI. ΔE is the intrinsic theoretical bandwidth.

Crystal #	Growth technique	Surface plane	Diameter/Thickness(mm)	Reflection	Energy (keV)	Extinction length(μm)	ΔE (meV)
1	Kyropoulos	(0001)	22/1	$0\ 1\ \bar{1}\ 50$	23.905	145	1.57
2	Kyropoulos	$(01\bar{1}2)$	40/1.1	$7\ 10\ \overline{17}\ 18$	23.858	130	1.71
3	Bridgman	(0001)	27/2.5	$0\ 1\ \bar{1}\ 50$	23.905	145	1.57
4	Kyropoulos	(0001)	30/1	$0\ 1\ \bar{1}\ 50$	23.905	145	1.57
5	Kyropoulos	$(10\bar{1}2)$	30/3	$7\ 10\ \overline{17}\ 18$	23.858	130	1.71

channel-cut crystals in the nested design where Si(6 4 2) reflections with asymmetry parameter $b = -0.043$ are chosen for the outer channel-cut crystal and symmetric Si(12 12 12) reflections are chosen for the inner channel-cut crystal. The energy of the HRM was chosen between 23.840 and 23.905 keV in order to match the sapphire backscattering reflections listed in Table I. For this energy range, the theoretical energy bandwidth of the HRM is obtained by numerical calculations between 0.63 meV and 0.73 meV dependent on the incoming beam divergence. Experimentally, a bandwidth of 0.9 meV has been measured using nuclear resonance scattering by ^{119}Sn at 23.88 keV. The deviation from the theoretical value is due to the imperfections of the Si crystals across the beam spot, and an energy bandwidth of 0.7 meV is expected for small parts of the beam, as seen by individual 55 μm size pixels of the detector, see below.

In order to cover a large area on the investigated crystals, the beam downstream of the HRM has been enlarged in the vertical direction by using two asymmetric Si(111) reflections with combined asymmetry parameter, $b_{\text{total}} = 10$. Due to the large angular width of these reflections, they do not modify the energy resolution for the HRM. The beam at the studied crystals had a size of $\sim 1.9 \times 2.5$ mm^2 (H × V) FWHM. The beam back-reflected by the sapphire, installed in near backscattering geometry with a Bragg angle θ_B of 89.90° was collected by a two-dimensional MaxiPix detector, with 55×55 μm^2 pixel size. The intensity in each pixel was measured as a function of incoming energy tuned by the HRM with an energy step of 0.5 meV while the sapphire crystal stayed at rest and constant temperature. Thus, a set of rocking curves for 4×3.5 mm^2 (H × V) spots on the sapphire crystal were obtained with a spatial resolution of 55 μm. The data sets were analyzed and maps of the rocking curve width and of the maximum position were recorded. In order to characterize the entire surface, the crystal was moved in the transverse directions relative to the beam, and the same measurements were repeated.

The theoretical rocking curve widths for the ideal crystals were calculated numerically taking into account all crystals in the optical setup and incoming beam divergence of 15 μrad expected at this energy at the beamline ID18. However, the dependence of the widths on incoming beam divergence is very small, as expected for this setup.

III. RESULTS

The map of the rocking curve widths measured by RCI for crystal #1 is shown in Fig. 2(a). The straight line (pointed at by the tip of the black filled arrow) and the yellow area below it are artifacts caused by diffraction from the sample holder. The map shows that the width in most of the crystal regions varies between 3.0 and 4.0 arcsec, which is comparable with the value estimated for an ideal crystal and ideal optical setup. Thus, for most of the crystal regions, the broadening of the reflection is not more than 30% of the ideal width. The reasonable quality with a precision of $\delta d/d = 10^{-4}$ is also confirmed by the rocking curves shown in Fig. 2(b). These rocking curves were acquired at four individual spots, 1–4, in Fig. 2(a) and normalized to the maximum intensity. The rocking curves at spots 1 and 2 have symmetric ideal shapes with widths of $\sim$3.6 arcsec. Almost the same width is observed for spot 3. Only the rocking curve at spot 4 shows broadening mainly due to the presence of two peaks corresponding to areas with different lattice spacings or with misorienation of the lattice planes. If this effect arises from variations in the lattice spacing, the lattice parameter variation can be estimated to be $\delta d/d \sim 1.6 \times 10^{-4}$.

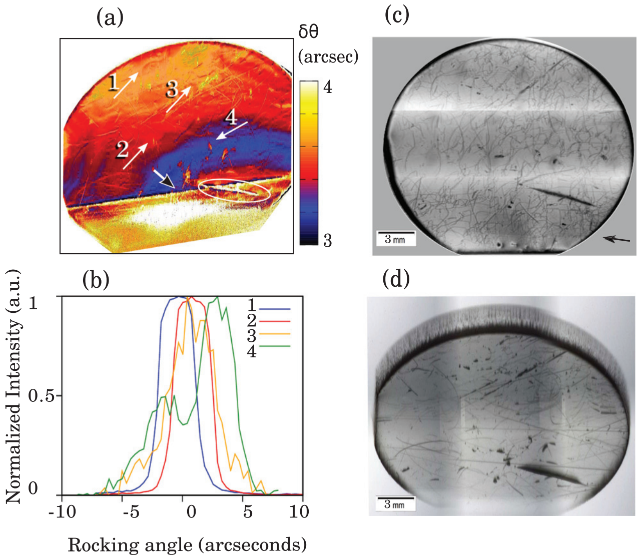

FIG. 2. (a) The map of the rocking curve widths obtained from crystal #1 using rocking curve imaging. The white arrows point to the region where rocking curves are displayed in panel (b), were measured and the black filled arrow points the artefact from the aluminium sample holder. The large crystal defect is shown inside the drawn ellipse. Blue denotes smaller width and red larger width. (b) Rocking curves obtained at spots labeled in (a). (c) White beam topograph in transmission, Laue, geometry, the black arrow shows the diffraction vector, **g**. (d) Monochromatic beam topograph recorded at the slope of the rocking curve with the rocking curve imaging setup in reflection, Bragg, geometry.

However, much higher sensitivity to defects can be obtained by an investigation of the topograph performed at the slope of the rocking curve.[39] The topograph of crystal #1 obtained in reflection, Bragg, geometry is shown in Fig. 2(d) together with the white beam topograph shown in Fig. 2(c). Both topographs show significant amounts of defects not visible in the map of rocking curve widths. The defects do not always correlate in both topographs. There can be several reasons for this. One reason is that white beam topography was used in transmission geometry and the other methods were used in reflection geometry. A second reason is related to extinction rules. A defect is only visible if it deforms the diffracting lattice planes (HKL). If the diffracting lattice planes are different, then one is sensitive (or insensitive) to different components of the strain-field of the given defect. So a direct consequence is that the visible or invisible details of a defect image need not be the same in two images obtained with a different diffraction condition (diffraction vector, normal to the diffraction plane). In Laue or transmission geometry, which we used in the case of white beam topography,[36] we may detect defects in the whole illuminated crystal volume, starting from the beam entrance surface to the exit surface. In Bragg or reflection geometry, which was used in the case of monochromatic beam topography, the intensity of the X-ray wave fields in the crystal plate decreases exponentially with the distance from the entrance surface. Consequently, in this last geometry, defects on or close to the entrance surface give more intense defect images than those close to the exit surface. The visibility of defects in deeper regions of the crystal plate depends on the reflection used, the energy of the X-rays used, the plate thickness, and the atomic numbers of the crystal components, that means, to a large degree, on the product of absorption coefficient times plate thickness. For the present conditions (low Z, rather high energy, rather thin crystal plate), the defects in deeper regions should still be visible.

In order to test the feasibility of the method, the backscattering RCI was first applied to a Ge crystal, which has almost ideal quality. Here, the Ge(5 15 15) reflection was used at an energy of 23.880 keV with an intrinsic width of 2.85 meV ($\delta E/E = 12 \times 10^{-8}$). For each pixel, the widths of the rocking curve and positions of the maximum of the curves were determined and the corresponding maps are displayed in Figs. 3(a) and 3(b) in units of relative lattice parameter variation, $\delta d/d$, which is equivalent to $\delta E/E$. In addition, examples of rocking curves obtained at a few labeled pixels are shown in Fig. 3(c). The width of the reflection is very uniform across the area with the exception of the lines (yellow color) where a larger width is observed. These lines are due to the scratches on the surfaces visible to the eye. The average value of the widths for good areas is 3.2 meV, which is close to the theoretical value of 3.0 meV obtained by numerical calculations. The position of the reflection maximum is also the same across the good areas of the crystal and shifted by up to 2 meV at the scratches. The lattice spacing close to the surface scratches is slightly different from that in the middle area of each zone. This is related to strain fields near the scratches that have similar consequences to those of intrinsic crystal defects. As can be seen from the bottom part of Fig. 3(a), these scratches are very close to each other, which actually make the strain-free parts rather small. The shift is due to the decrease of the lattice constant at the scratches on the order of $\delta d/d \sim 5 \times 10^{-8}$. This study shows that, indeed, this imaging backscattering topography setup can provide reliable information about crystal quality with a relative precision of 10^{-7}–10^{-8}.

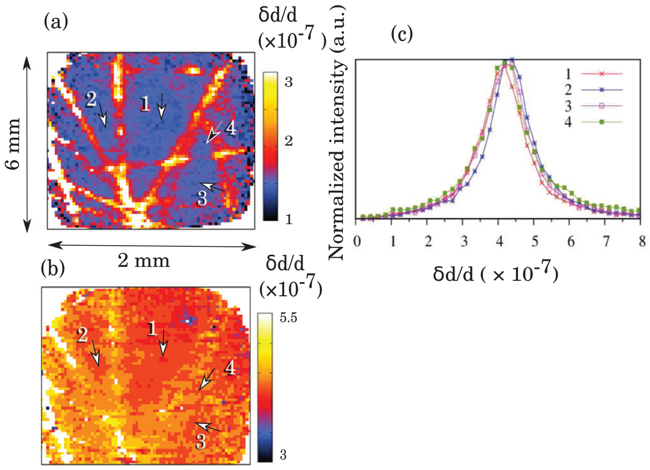

FIG. 3. Backscattering rocking curve imaging maps of a Ge crystal. (a) The map of the rocking curve widths in units of $|\delta d/d| = |\delta E/dE|$. (b) The map of the rocking curve centers in units of $\delta d/d$. (c) Rocking curves measured at the pixels labeled in (a) and (b).

Backscattering RCI was applied to characterize sapphire crystals using the reflections $(0\,1\,\bar{1}\,50)$ and $(7\,10\,\overline{17}\,18)$ with intrinsic widths of 1.5 and 1.7 meV, and similar extinction lengths, see Table I. Taking into account the 0.7 meV HRM bandwidth, the numerical calculations provide 1.59 meV and 1.77 meV energy widths for the reflectivity curves of the ideal crystals. Due to the rather large step of 0.5 meV in the scans of the rocking curves, the precision of the parameters' estimation is about 0.2 meV.

The backscattering topography maps of crystal #1 measured with reflection $(0\,1\,\bar{1}\,50)$ at an energy of 23.906 keV are shown in Fig. 4. The integrated intensity distribution on the detector is shown in Fig. 4(a) where the modulation by the beam intensity profile is visible for the ∼40 crystal positions. The rocking curve width map of the entire crystal is shown in Fig. 4(b). For a chosen spot denoted by the square frame in the full map in Fig. 4(b), a detailed map of the widths and of the energy distributions at the peak positions are shown in Figs. 4(c) and 4(d), respectively. Note that due to uncontrolled small drifts of the absolute energy of the HRM used in the experiment, we can compare the position of the maximum reflectivity curves only within one illuminated spot, among the ∼40 spots used to raster the crystal, where the energy is tuned simultaneously for all pixels in the detector.

The map of rocking curve widths reveals that the crystal quality varies strongly on a pixel by pixel base. Closer inspection reveals features similar to the white beam topography. For example, the big defect in the bottom right part of the topograph in Figs. 2(c) and 2(d) appears in white in the map in Fig. 4(b). Regions that only exhibit a few dislocations in the middle left part have the best resolution and are shown as dark blue. Examples of the rocking curves measured in the best and worst areas are presented in Figs. 4(e) and 4(f).

The detailed maps of Figs. 4(c) and 4(d) show that there are 4 spots of almost ideal quality with the characteristic edge length of 0.2–0.5 mm marked by numbers 1–4 in the figure. The quality of these spots is confirmed by the rocking curves taken at the spots and shown in Fig. 4(e). The characteristic width at these spots is $\delta d/d = 6 \times 10^{-8}$, i.e., an energy bandwidth of 1.43 meV. However, the peak position varies from point to point and a spread over $\delta d/d = 12 \times 10^{-8}$ can be seen between curves 3 and 4. Such variation of the lattice constant between almost ideal spots is two times larger than the width of the reflection. The bad quality of the reflections on the border between good spots is partly due to the overlap of the areas with different lattice parameters.

For crystal #2, the map of rocking curve widths was recorded with the reflection $(7\,10\,\overline{17}\,18)$ and is shown in Fig. 5(a). Only tiny areas exhibit a width $\delta d/d < 10 \times 10^{-8}$. The rest of the crystals is highly deformed mainly on the left side. A smaller region denoted by the white rectangle was selected and the corresponding width (Fig. 5(b)) was analyzed. The rocking curves in the center of the good spots are

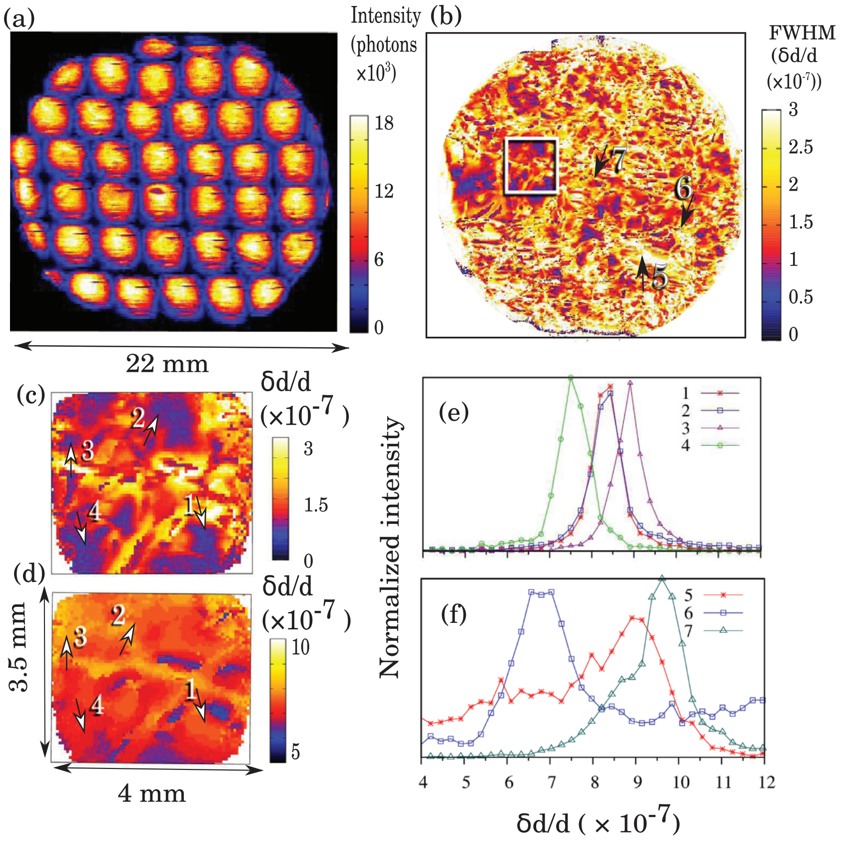

FIG. 4. The maps of backscattering rocking curve imaging of crystal #1. (a) Total intensity map obtained by integration of the flux over rocking curve. This map represents the beam profile. Different spots correspond to the different positions of the crystal. (b) The map of the rocking curve widths in units of $|\delta d/d| = |\delta E/E|$. (c) A part of this width map in (b) at one crystal position, marked by the white square in (b). (d) The map of the rocking curve centers in units of $\delta d/d$ for the same area as in (c). (e) and (f) Rocking curves measured at the pixels labeled by numbers in (b) and (c).

shown in Fig. 5(c). The good spots have an edge length of 0.2–0.5 mm. These rocking curves are symmetric and without any satellite peaks, similar to the first crystal. An average width of about 8×10^{-8} was obtained, corresponding to 2.0 meV. This value is close to the expected 1.8 meV for an ideal crystal. However, again the peak positions are spread in a range of 50×10^{-8}, 6 times larger than the width of the reflection, see the peak position map in Fig. 5(d).

The maps for crystal #3 are shown in Fig. 6. The reflection $(0\,1\,\bar{1}\,50)$, as for crystal #1, was used here. However,

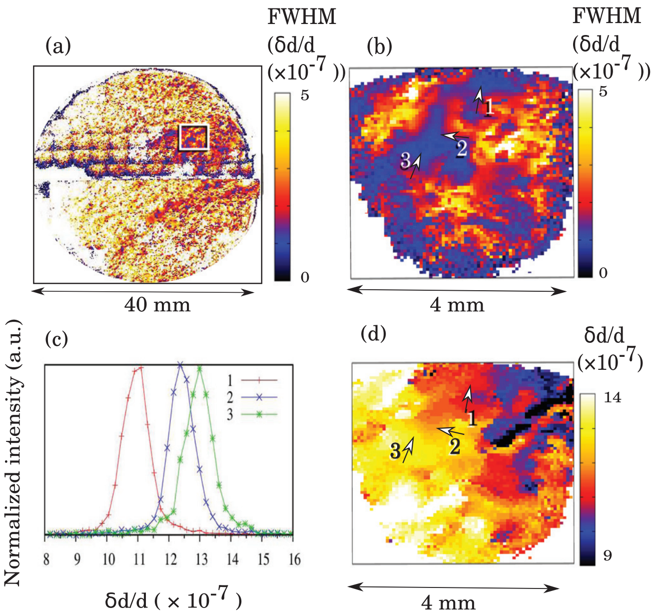

FIG. 5. Backscattering rocking curve imaging maps of crystal #2. (a) The map of the rocking curve widths. (b) The map of the rocking curve widths taken for one crystal position marked by the white square in (a). (c) Rocking curves measured at the pixels labeled by numbers 1, 2, and 3 in (b). (d) The map of back reflection peak positions of the rocking curves taken for one crystal position marked by the white square in (a).

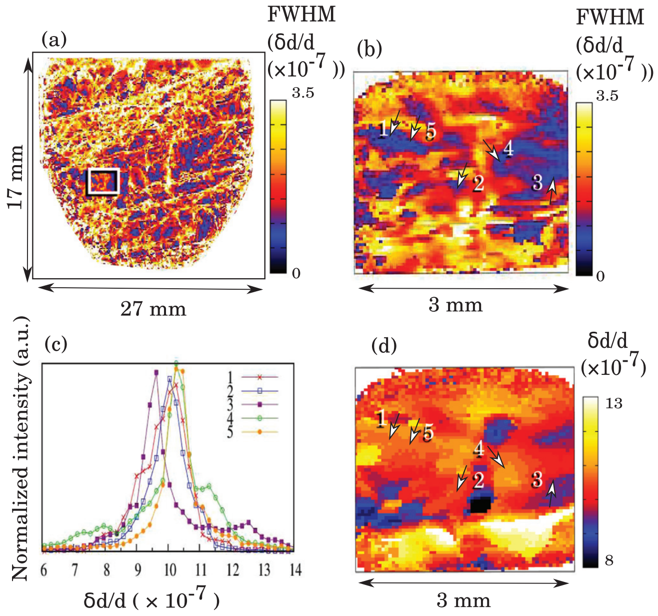

FIG. 6. Backscattering rocking curve imaging maps of crystal #3. (a) The map of the rocking curve widths. (b) The map of the rocking curve widths in the area marked by the white square in (a). (c) Rocking curves measured at the pixels labeled by numbers 1, 2, 3, 4, and 5 in (b). (d) The map of back reflection peak positions of the rocking curves taken for the same area as (b).

this crystal was grown by a different method, see Sec. IV and Table I. High quality spots with area with an edge length of 0.2–0.5 mm are distributed over almost the entire crystal. They are separated by bad quality interface lines due to the scratches on the surface. The rocking curves from good areas in one frame are compared in Fig. 6(c). Most of these rocking curves have an asymmetric shape with satellite peaks. The average width of these curves is determined to be about $\delta d/d = 9 \times 10^{-8}$ or 2.3 meV, which is 50% larger than theoretically expected for an ideal crystal. A peak position spread is also observed for the selected narrow rocking curves. However, the characteristic spread value $\delta d/d = 3 \times 10^{-8}$ is smaller than in the other crystals of this study. The measurements of crystals #4 and #5 indicate comparatively poor quality of these crystals, see Fig. 7.

IV. DISCUSSION

As seen by RCI in Fig. 2, crystal #1 is comprised of large areas with rocking curve widths of $\leq$4 arcsec, which signifies almost uniform quality at a resolution level of $\delta d/d \sim 10^{-4}$. Typically, the average widths of the rocking curve of crystals with medium-high quality are a few tens of arcsec.[30,40] However, with the technology developed in the last decade, widths as good as 9.43 arcsec (Ref. 2) and 8.7 arcsec (Ref. 41) have been achieved. The latter result was achieved with crystals grown by the Rubicon Technology Inc. company, measured with reflection (0 0 0 6) (Bragg angle of 21°) at 8 keV.

A much higher resolution level of $\delta d/d \sim 7 \times 10^{-8}$ is provided by RCI in backscattering geometry where resolution is defined by the width of the rocking curve. In addition, a spatial resolution of 55 μm was obtained over the entire crystal surface. Accordingly, the more than 3 orders of magnitude higher strain sensitivity reveals the presence of heterogeneous defects or grown in local stresses within each of the samples that are not detectable with the $\sim$$10^{-4}$ strain sensitivity of RCI. Several spots of almost ideal quality and with an edge length of 0.2–0.5 mm were found in the maps of all crystals. In principle, such spots can be used for efficient monochromatization of the X-ray beams by using a focused incoming beam. However, most of the crystal areas have worse quality with broadening of the reflectivity curves up to $\delta d/d \sim 3\text{–}5 \times 10^{-7}$. Such quality would lead to an energy bandwidth of the monochromator at 35 keV of about 10–18 meV, which is not acceptable for NIS. However, such quality could be reasonable for analyzers used in RIXS, since it would provide an energy bandwidth of 5 meV, for the X-ray energy of 10 keV.

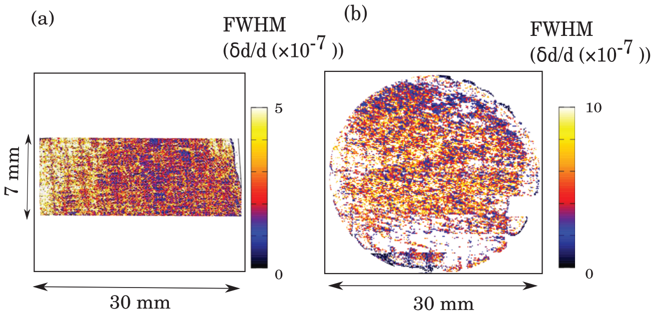

FIG. 7. The maps of rocking curve widths of (a) part of crystal #4 recorded at reflection (0 1 $\bar{1}$ 50) and (b) crystal #5 recorded at reflection (7 10 $\overline{17}$ 18) using the backscattering rocking curve imaging setup.

Whereas good spots with symmetric rocking curves exist in all crystals, their quality is slightly different. The highest quality is obtained for the crystals #1 and #2 grown by the Kyropoulos method. The crystal #3 grown by the Bridgman method shows the rocking curve $\sim$50% broader compared to the theoretical expectation.

In addition to the width of the rocking curves, we also obtained the peak positions over the crystal area. We found that even for good spots the peak positions are different due to variations in the lattice parameters, which lead to characteristic variations at $\delta d/d \sim 10\text{–}20 \times 10^{-8}$. In a crystal with dislocations, lattice planes far from the dislocation could be subjected to a homogeneous stress that reduces the d-spacing with respect to a perfect crystal. Conversely, tensile stress would increase the d-spacing. The compressed lattice planes diffract the beam at a lower wavelength or higher energy. We can estimate the relative stress between the dislocation-free regions in crystal #1 along the beam direction, i.e., normal to the C plane, because the chosen $(0\,1\,\bar{1}\,50)$ reflection is nearly perpendicular to the surface. The internal stress (σ) in the crystal can be derived from the lattice strain ($\delta d/d$) and elastic tensor c according to $\sigma = c \cdot \delta d/d$. A relative stress of 40(5) kPa is obtained from the relative shift in the position of peaks 3 and 4 in Fig. 4(e) considering the c_{33} elastic constant from Refs. 42 and 43. According to numerical simulations, due to thermoelastic stress during growth the best part of a Kyropoulos grown boule exhibits an absolute stress value similar to 600 kPa.[44] However, most parts of the crystal exhibit values in the range of MPa to GPa.[26,44,45] A numerical study on thermoelastic stress distributions for silicon grown by a similar technique, the Czochralski method, calculates the stress values between a few MPa and 40 MPa,[46] much smaller than typical in sapphire. So, not only the average stress in the crystal must be lowered but also its relative change throughout the crystal must be reduced before sapphire crystals, which can be considered as perfect for X-ray optics, can be grown.

The data gathered in this study also suggest that crystals with surface oriented perpendicular to $[0\,0\,0\,1]$ have less X-ray visible lattice defects than those cut perpendicular to $[0\,1\,\bar{1}\,2]$ and $[1\,0\,\bar{1}\,2]$ directions. The Kyropoulos technique is known as an effective method to grow sapphire crystals with high quality, especially in large diameters.[2] Nevertheless, a comparison of crystals #1 and #4 shows that the quality of crystals grown by the same conditions changes dramatically. This is likely due to the inability to control all the known parameters such as the growth rate and temperature gradient or other unidentified parameters.

The impact of discrete dislocations on the lattice parameter variations was investigated by comparison of the white beam topographs and the map of widths in crystal #1 as shown in Fig. 8. Here, blue, red, and black contours shows regions with widths of 2, 4, and 6 meV in the map of the rocking curve widths plotted on top of the white beam topograph. In general, the higher the density of defects visible in

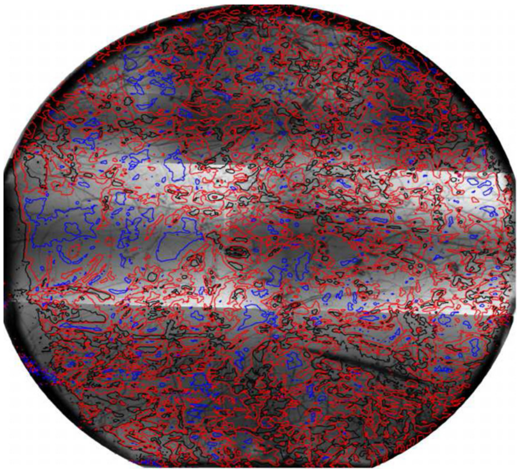

FIG. 8. Overlay map of the white beam topograph and the map of rocking curve widths for crystal #1 obtained from white beam transmission topography and backscattering rocking curve imaging, respectively. The blue, red, and black contours are drawn for widths of 2, 4, and 6 meV in the map of rocking curve widths, respectively.

topographs, the poorer the quality of the reflections. At the same time, the best resolutions in the rocking curve widths map do not necessarily signify the absence of defects. The reason for this disagreement is the limited depths of the backscattering reflection. The extinction length of the $(0\,1\,\bar{1}\,50)$ reflection is 145 μm at 23.9 keV, which is smaller than the 1 mm thickness of the crystal. Thus, defects inside the crystal cannot be detected by backscattering topography but are visible in the white beam transmission topograph. In order to check the distribution of defects through the depth of the crystal, backscattering topography on the crystal #1 has been performed from both sides. It was found that the maps of the rocking curve widths from both sides are, in general, similar, so that the density of the defects is uniform through the crystal. However, these results do not exclude the presence of deeper defects in the bulk of crystal to which backscattering topography is not sensitive. These defects would be visible with backscattering topography at higher energy.

In addition to the material-specific insights that we obtained on sapphire crystals, another result is the demonstration of high throughput rocking curve imaging in backscattering geometry. The measurement duration is short, e.g., scanning a 20 mm diameter crystal takes about an hour. This is the technique of choice for determining lattice parameter variations with a high sensitivity of $\delta d/d \approx 10^{-8}$ in nearly perfect single crystals. Note that the sensitivity could be improved by the choice of a narrower bandwidth monochromator, such as discussed in Ref. 47. The resolution can be improved further using differential intensity measurements at the slope of the rocking curve as often used for topography.[33,48] Assuming the best intensity resolution of $\delta I/I \sim 0.05$, we estimate that the backscattering topography method with the HRM used here can provide a $\delta d/d$ resolution down to 10^{-10}.

In this modified topography-like setup, tuning the energy of the incident beam instead of rocking through the Bragg angle of the crystal provides direct access to lattice parameter variation and reveals changes in the peak position of rocking curves with high precision. Another advantage of the setup used is the relatively large beam size obtained by combining a magnifying arrangement of asymmetrically cut crystals together with a large area pixel detector, a combination which provides a solution for utilizing backscattering geometry RCI imaging map in large areas in a reasonable time at a synchrotron radiation facility. We note that this technique can in principle be applied in a larger energy range, not restricted to specific nuclear resonance energies. The only requirement is the construction of a HRM with meV bandwidth, which is now possible between 6 and 30 keV. For the purpose of backscattering RCI, in contrast to nuclear resonance scattering, the HRM energy can be chosen freely and the method does not require very high flux. Thus, an extension to higher energies is possible.

V. CONCLUSION

In this study, X-ray characterization of several high quality sapphire single crystals has been performed using three methods: white beam topography, RCI, and backscattering RCI. The RCI results show the crystals to be of almost uniformly good quality at a lattice parameter resolution of $\delta d/d \sim 10^{-4}$, typically sufficient for visible light applications. At the same time, backscattering RCI with resolution $\delta d/d \sim 5 \times 10^{-8}$ reveals mixed quality through all crystals. Nearly ideal regions with an edge length of 0.2–0.5 mm were found. However, the lattice parameter even for the ideal spots varies in the range of $\delta d/d = 10\text{–}50 \times 10^{-8}$, which is a few times larger than the width of the reflection. We attribute this variation of the lattice parameters to the presence of regions with local stresses of ~40 kPa generated during crystal growth. Stresses of this magnitude must be expected with the current procedure of sapphire growth. Thus, in order to obtain sapphire crystals of sufficient quality for X-ray high resolution monochromators or analyzers, the crystal growth procedure has to be improved in order to decrease the relative thermoelastic stress.

ACKNOWLEDGMENTS

We are grateful to the Helmholtz association of German Research Centers and the Russian Academy of Science for supporting the projects HRJRG-402 "Sapphire ultra optics for synchrotron radiation "and DFG SFB-917" nanoswitches." R.P.H. acknowledges support from the Materials Sciences and Engineering Division, Office of Basic Energy Sciences, U.S. Department of Energy. D.B. acknowledges financial support from the Industrial Partnership Program (IPP-I28) of Foundation for Fundamental Research on Matter (FOM) (The Netherlands) and BASF New Business. We acknowledge the ESRF, ANKA, and DESY for provision of synchrotron radiation beamtimes. We are also immensely grateful to Andreas N. Danilewsky for all the help provided and John Budai and Ben Larson for helpful comments.

[1] M. N. Ediger, R. W. Waynant, N. I. Djeu, Y. Shimoji, and R. S. F. Chang, in *Proceedings of the Annual International Conference of the IEEE*

Engineering in Medicine and Biology Society, 1989. Images of the Twenty-First Century (1989), Vol. 4, p. AP/1.

[2] H. Tang, H. Li, and J. Xu, *Growth and Development of Sapphire Crystal for LED Applications* (INTECH Open Access Publisher, 2013).

[3] H. Schumacher, T. J. Gmitter, H. P. LeBlanc, R. Bhat, E. Yablonovitch, and M. A. Koza, Electron. Lett. **25**, 1653 (1989).

[4] F. J. Bruni, Cryst. Res. Technol. **50**, 133 (2015).

[5] J. Hrdý and O. Pacherová, Nucl. Instrum. Methods Phys. Res., Sect. A **327**, 605 (1993).

[6] C. David, J. Bruder, T. Rohbeck, C. Grnzweig, C. Kottler, A. Diaz, O. Bunk, and F. Pfeiffer, "Fabrication of diffraction gratings for hard X-ray phase contrast imaging," in *Proceedings of the 32nd International Conference on Micro- and Nano-Engineering* (2006), [Microelectron. Eng. **84**, 1172 (2007)].

[7] Y. Shvyd'ko and E. Gerdau, Hyperfine Interact. **123**, 741 (1999).

[8] A. J. Rondinone, C. Y. Jones, S. L. Marshall, B. C. Chakoumakos, C. J. Rawn, and E. Lara-Curzio, Can. J. Phys. **81**, 381 (2003).

[9] J. Kohlbrecher, A. Bollhalder, R. Vavrin, and G. Meier, Rev. Sci. Instrum. **78**, 125101 (2007).

[10] S. Bayya, G. Villalobos, W. Kim, J. Sanghera, M. Hunt, and I. D. Aggarwal, "Rugged sensor window materials for harsh environments," Proc. SPIE **9202**, 92021D (2014).

[11] J. B. Taylor, R. Boland, E. Gowac, P. Stupik, and M. Tricard, "Recent advances in high-performance window fabrication," Proc. SPIE **8708**, 870816 (2013).

[12] T. Gog, D. M. Casa, A. H. Said, M. H. Upton, J. Kim, I. Kuzmenko, X. Huang, and R. Khachatryan, J. Synchrotron Radiat. **20**, 74 (2013).

[13] Y. Shvyd'ko, *X-Ray Optics-High-Energy-Resolution Applications*, Springer Series in Optical Sciences Vol. 98 (Springer, Berlin, 2009).

[14] S. Tsutsui, Y. Yoda, and H. Kobayashi, J. Phys. Soc. Jpn. **76**, 065003 (2007).

[15] H.-C. Wille, R. P. Hermann, I. Sergueev, U. Pelzer, A. Möchel, T. Claudio, J. Perßon, R. Rüffer, A. Said, and Y. V. Shvyd'ko, EPL **91**, 62001 (2010).

[16] I. Sergueev, H.-C. Wille, R. P. Hermann, D. Bessas, Y. V. Shvyd'ko, M. Zajac, and R. Rüffer, J. Synchrotron Radiat. **18**, 802 (2011).

[17] H.-C. Wille, R. P. Hermann, I. Sergueev, O. Leupold, P. van der Linden, B. C. Sales, F. Grandjean, G. J. Long, R. Rüffer, and Y. V. Shvyd'ko, Phys. Rev. B **76**, 140301 (2007).

[18] B. Klobes, A. Desmedt, I. Sergueev, K. Schmalzl, and R. P. Hermann, EPL **103**, 36001 (2013).

[19] R. Rüffer and A. I. Chumakov, Hyperfine Interact. **97**, 589 (1996).

[20] H.-C. Wille, Y. V. Shvyd'ko, E. E. Alp, H. D. Rüter, O. Leupold, I. Sergueev, R. Rüffer, A. Barla, and J. P. Sanchez, EPL **74**, 170 (2006).

[21] Y. Imai, Y. Yoda, S. Kitao, R. Masuda, S. Higashitaniguchi, C. Inaba, and M. Seto, Proc. SPIE **6705**, 670512 (2007).

[22] E. Dobrovinskaya, L. Lytvynov, and V. Pishchik, *Sapphire: Material, Manufacturing, Applications*, Micro- and Opto-Electronic Materials, Structures, and Systems (Springer, USA, 2009).

[23] P. Rudolph, *Handbook of Crystal Growth: Bulk Crystal Growth* (Elsevier Science, 2014).

[24] S. E. Demina, E. N. Bystrova, M. A. Lukanina, V. M. Mamedov, V. S. Yuferev, E. V. Eskov, M. V. Nikolenko, V. Postolov, and V. V. Kalaev, Opt. Mater. **30**, 62 (2007).

[25] D. C. Harris, "A century of sapphire crystal growth: Origin of the EFG method," Proc. SPIE **7425**, 74250P (2009).

[26] X. Chenghai, M. Songhe, Z. Mingfu, Z. Hongbo, and W. Guigen, Chin. J. Aeronaut. **20**, 475 (2007).

[27] M. S. Akselrod and F. J. Bruni, in *5th International Workshop on Crystal Growth Technology* (2011) , [J. Cryst. Growth **360**, 134 (2012)].

[28] E. R. Dobrovinskaya, L. A. Lytvynov, and V. Pishchik, *Sapphire Material, Manufacturing, Applications* (Springer, Berlin, 2009).

[29] L. S. Birks, J. W. Hurley, and W. E. Sweeney, J. Appl. Phys. **36**, 3562 (1965).

[30] P. M. Adams, *Evaluation of the Quality of Sapphire Using X-Ray Rocking Curves and Double-Crystal X-Ray Topography* (PN, 1994), pp. 1–17.

[31] Y. Wang, S. Liu, G. Peng, S. Zhou, and J. Xu, J. Cryst. Growth **274**, 241 (2005).

[32] D. Lübbert, T. Baumbach, J. Härtwig, E. Boller, and E. Pernot, Nucl. Instrum. Methods Phys. Res., Sect. B **160**, 521 (2000).

[33] M. Hart, J. Cryst. Growth **55**, 409 (1981).

[34] J. P. Sutter, A. Q. R. Baron, D. Miwa, Y. Nishino, K. Tamasaku, and T. Ishikawa, J. Synchrotron Radiat. **13**, 278 (2006).

[35] Y. Shvyd'ko, Nat. Phys. **6**, 196 (2010).

[36] V. E. Asadchikov, A. V. Butashin, A. V. Buzmakov, A. N. Deryabin, V. M. Kanevsky, I. A. Prokhorov, B. S. Roshchin, Y. O. Volkov, D. A. Zolotov, A. Jafari, P. Alexeev, A. Cecilia, T. Baumbach, D. Bessas, A. N. Danilewsky, I. Sergueev, H.-C. Wille, and R. P. Hermann, Cryst. Res. Technol. **51**, 290 (2016).

[37] D. Lübbert and T. Baumbach, J. Appl. Crystallogr. **40**, 595 (2007).

[38] A. I. Chumakov, A. Barla, R. Rüffer, J. Metge, H. F. Grünsteudel, H. Grünsteudel, J. Plessel, H. Winkelmann, and M. M. Abd-Elmeguid, Phys. Rev. B **58**, 254 (1998).

[39] B. Tanner, *X-Ray Diffraction Topography: International Series in the Science of the Solid State* (Elsevier Science, 2013).

[40] P. Capper, *Bulk Crystal Growth of Electronic, Optical and Optoelectronic Materials, Wiley Series in Materials for Electronic & Optoelectronic Applications* (Wiley, 2005).

[41] J. P. Ciraldo, J. Levine, and H. Ganegoda, Proc. SPIE **9100**, 91000Q (2014).

[42] J. B. Watchman, W. E. Teffet, D. G. Lam, and R. P. Stinchfield, J. Am. Ceram. Soc. **43**, 334 (1960).

[43] J. H. Gieske and G. R. Barsch, Phys. Status Solidi B **29**, 121 (1968).

[44] S. Demina, E. Bystrova, V. Postolov, E. Eskov, M. Nikolenko, D. Marshanin, V. Yuferev, and V. Kalaev, in *Proceedings of the 15th International Conference on Crystal Growth (ICCG-15) in conjunction with the International Conference on Vapor Growth and Epitaxy and the US Biennial Workshop on Organometallic Vapor Phase Epitaxy* (2007), [J. Cryst. Growth **310**, 1443 (2008)].

[45] Z. Jin, H. Fang, N. Yang, Z. Zhang, S. Wang, and J. Xu, J. Cryst. Growth **405**, 52 (2014).

[46] A. Benmeddour and S. Meziani, Revue des Energies Renouvelables **12**, 575 (2009).

[47] T. S. Toellner, J. Collins, K. Goetze, M. Y. Hu, C. Preissner, E. Trakhtenberg, and L. Yan, J. Synchrotron Radiat. **22**, 1155 (2015).

[48] A. Authier, *Dynamical Theory of X-ray Diffraction*, IUCr Monographs on Crystallography (Oxford University Press, 2004).